# Magnetic control of Weyl nodes and wave packets in three-dimensional warped semimetals

Bruno Focassio,[1] Gabriel R. Schleder,[1] Adalberto Fazzio,[2] Rodrigo B. Capaz,[1,3] Pedro V. Lopes,[3] Jaime Ferreira,[4] Carsten Enderlein,[5] and Marcello B. Silva Neto[3,1]

[1]*Laboratório Nacional de Nanotecnologia, LNNano/CNPEM, 13083-100 Campinas, São Paulo, Brazil*

[2]*Ilum School of Science, CNPEM, 13083-970 Campinas, São Paulo, Brazil*

[3]*Instituto de Fisica, Universidade Federal do Rio de Janeiro, Caixa Postal 68528, Rio de Janeiro, Brazil*

[4]*Centro Brasileiro de Pesquisas Físicas, Rua Dr. Xavier Sigaud, 22290-180 Rio de Janeiro, Brazil*

[5]*Instituto de Fisica, Universidade Federal do Rio de Janeiro, Campus Duque de Caxias, 25245-390 Rio de Janeiro, Brazil*

(Received 29 January 2024; accepted 21 August 2024; published 12 September 2024)

We investigate the topological phase transitions driven by band warping, $\lambda$, and a transverse magnetic field, $B$, for three-dimensional Weyl semimetals. First, we use the Chern number as a mathematical tool to derive the topological $\lambda \times B$ phase diagram. Next, we associate each of the topological sectors to a given angular momentum state of a rotating wave packet. Then we show how the position of the Weyl nodes can be manipulated by a transverse external magnetic field that ultimately quenches the wave packet rotation, first partially and then completely, thus resulting in a sequence of field-induced topological phase transitions. Finally, we calculate the current-induced magnetization and the anomalous Hall conductivity of a prototypical warped Weyl material. Both observables reflect the topological transitions associated with the wave packet rotation and can help to identify the elusive 3D quantum anomalous Hall effect in three-dimensional, warped Weyl materials.

DOI: 10.1103/PhysRevResearch.6.033289

## I. INTRODUCTION

Wave packets are one of the most fundamental objects in quantum mechanics [1]. Schrödinger introduced them [2] right after the publication of his famous wave equation, inspired by the wave-particle duality proposed by de Broglie [3]. One hundred years later, the de Broglie-Mackinnon wave packet has been finally observed, using paraxial space-time-coupled pulsed laser fields in the presence of anomalous group-velocity dispersion [4]. Optical wave packets that are localized in space and time have also found applications ranging from microscopy and remote sensing, to nonlinear and quantum optics [5]. Localized coherent phonon wave packets are being launched by ultrafast Coulomb forces in a scanning tunneling microscope using tip-enhanced terahertz electric fields [6]. Ultrasonic acoustic wave packets have beaten the diffraction limit in the far-field for ultrasound waves [7]. Finally, matter wave packets can be optically manipulated for applications in ultrafast electron microscopy [8]. Having a finite Compton wavelength, wave packets can rotate about its own center of mass axis with a given orbital angular momentum and thus carry an intrinsic vorticity.

Optical vortices are paraxial vortex light beams possessing a Hilbert factor, $e^{i\ell\phi}$ [9], a phase singularity with a nonzero topological charge, $\ell$, which gives rise to a hollow intensity distribution (dark spot) and a phase front that describes a helix about the axis of propagation, $\mathbf{k}$ [10]. The topological charge $\ell$ (also called the winding number) quantizes this winding such that there is a phase change of $2\pi\ell$ during a full rotation. This $e^{i\ell\phi}$ factor is also a characteristic feature of orbital angular momentum (similar to the azimuthal phase in the hydrogenic wave functions), and is not restricted to light beams. Phonons may acquire a nonzero angular momentum due to forces induced by the relative displacements of atoms out of their equilibrium positions [11]. Ultrasonic vortex beams have been shown experimentally to be obliquely reflected off a flat water-air interface, confirming the theoretically predicted reversals of phase rotation, topological charge, and orbital angular momentum in a reflected vortex beam [12]. Freely propagating electron beams have been also produced in laboratory, whose wave front has a quantized topological structure arising from a singularity in phase, also taking the Hilbert form, $e^{i\ell\phi}$, with $\phi$ as the azimuthal angle about the beam axis and $\ell$ the topological charge [13]. Remarkably, the angular momentum of an electron vortex beam can be manipulated by an external magnetic field and exhibits well-known magnetic manifestations such as Stern-Gerlach transport, Larmor precession, Aharonov-Bohm phases, Landau energy levels, and Zeeman splitting [14].

Quite recently, the universal mapping of topological singularities in $\mathbf{k}$ space to measurable topological observables in real space has been demonstrated [15]. The mapping is based on the spin-orbit interaction, angular momentum conservation, and the nontrivial winding of the Berry phase, and is fundamentally of topological origin. The spin-orbit interaction leads to a Berry curvature having a monopole structure, $\mathcal{F}(\mathbf{k}) = \mathbf{k}/|\mathbf{k}|^3$ [16], which in turn, leads to the accumulation of the Berry phase about the linear momentum, $\mathbf{k}$, thus

shifting the relative phase of the plane waves and modifying the orbital angular momentum [13]. Although the mapping was demonstrated for the photonic honeycomb and Lieb lattices with vortex beams [15], the mechanism is universal and also works for rotating wave packets in three-dimensional (3D) Weyl systems [15].

In this work, we propose that the topological singularities of a nonmagnetic, 3D Weyl semimetal, with warping, $\lambda$, can be manipulated by an external magnetic field, $B$, due to its coupling to the wave packet orbital angular momentum. Weyl semimetals are ideal for this kind of manipulation, because while the robustness of Weyl nodes is ensured by topology [17], their positions can be easily fine tuned by external perturbations [18–20]. In fact, magnetic fields are being used to control the positions of the Weyl nodes and the emergence of the anomalous Hall or Nernst effects in magnetic semimetals [21–23]. Here we demonstrate that, while $\lambda$ brings Weyl nodes closer together, contributing to the Berry curvature, $\boldsymbol{\mathcal{F}}(\mathbf{k})$, and to the wave packet rotation, a transverse magnetic field pushes the nodes away, quenching the rotation of the wave packet. This leads to a rich $\lambda \times B$ topological phase diagram and to fingerprints in transport that can help to identify the 3D quantum anomalous Hall effect, when a magnetization is induced.

## II. WARPING AND TOPOLOGY

Weyl semimetals are characterized by a linear dispersion, $E(\mathbf{k}) = \pm|\mathbf{k}|$, a band crossing at a Weyl node, $\mathbf{k} = 0$, and a topological charge, $Q = \pm 1$. They are expected for systems where accidental band crossings occur and have indeed been observed for example in TaAs [24]. Multi-Weyl semimetals are characterized by a nonlinear dispersion, $E(\mathbf{k}) = \pm\sqrt{k_z^2 + k_\perp^{2\ell}}$, a band crossing at a multi-Weyl node, ($k_\perp^\ell = 0, k_z = 0$), and a topological charge, $Q = \pm\ell$. The existence of such multi-Weyl systems is guaranteed by point group symmetry [25] and they have been experimentally observed and studied in photonic crystals [26,27]. Mixed, multi-Weyl semimetals can be constructed with a low-energy Hamiltonian

$$\mathcal{H}_0 = \begin{bmatrix} k_z & k_- - \lambda k_+^2 \\ k_+ - \lambda k_-^2 & -k_z \end{bmatrix}, \tag{1}$$

therefore mixing up different topological sectors, $Q = \pm 1$ ($\lambda < \lambda_c$) and $Q = \mp 2$ ($\lambda > \lambda_c$), depending on the relative size of the warping parameter, $\lambda$, to the typical length scale associated to Weyl particles, the Compton wavelength, $\lambda_c$. This type of warping is a common feature in systems like monolayer graphene with Rashba spin-orbit coupling [28], twisted bilayer graphene [29], anomalous Hall materials [30], monolayer $MoS_2$ [31], elemental Te [32,33], and in $Bi_2Te_3$ [34].

Hamiltonian (1) can also be written as

$$\mathcal{H}_0 = \mathbf{d}(\mathbf{k}) \cdot \sigma, \tag{2}$$

where $\mathbf{d}(\mathbf{k}) = (d_x(\mathbf{k}), d_y(\mathbf{k}), d_z(\mathbf{k}))$ with

$$\begin{aligned} d_x(\mathbf{k}) &= k_x - \lambda\left(k_x^2 - k_y^2\right), \\ d_y(\mathbf{k}) &= k_y + 2\lambda k_x k_y, \\ d_z(\mathbf{k}) &= k_z, \end{aligned} \tag{3}$$

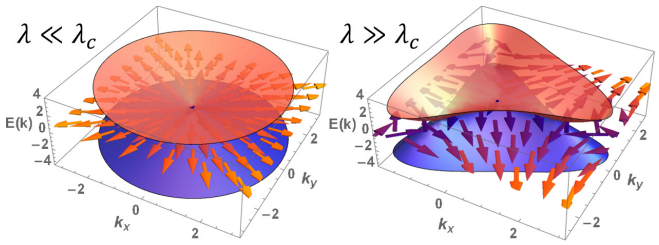


FIG. 1. Positive (red) and negative (blue) branches of the warped band dispersions, $E_\pm(\mathbf{k})$, for the limiting cases, $\lambda \ll \lambda_c$ (left) and $\lambda \gg \lambda_c$ (right), and the associated orbital magnetic textures at $k_z = 0$.

whose eigenvalues, $E_\pm(\mathbf{k}) = \pm|\mathbf{d}(\mathbf{k})|$, are shown in Fig. 1. The eigenstates of the Hamiltonian (1) are

$$|u_\mathbf{k}^\pm\rangle = \frac{1}{\sqrt{2|\mathbf{d}(\mathbf{k})|(|\mathbf{d}(\mathbf{k})| \mp d_z(\mathbf{k}))}} \begin{bmatrix} d_\mp(\mathbf{k}) \\ |\mathbf{d}(\mathbf{k})| \pm d_z(\mathbf{k}) \end{bmatrix}, \tag{4}$$

where $d_\pm(\mathbf{k}) = d_x(\mathbf{k}) \pm i d_y(\mathbf{k})$, which allows us to calculate the magnetic texture,

$$\mathbf{m}_\pm(\mathbf{k}) = \langle u_\mathbf{k}^\pm | \boldsymbol{\sigma} | u_\mathbf{k}^\pm \rangle = \pm \frac{\mathbf{d}(\mathbf{k})}{|\mathbf{d}(\mathbf{k})|}, \tag{5}$$

whose $k_z = 0$ profile is also shown in Fig. 1.

We will now construct a coherent wave packet following the general procedure described in [35]. Since the angular momentum, $\langle L_z \rangle$, of a rotating wave packet of size $\lambda_c$ in real space is universally determined by the total topological charge, $\ell$, within an envelope of size $k_c \sim 1/\lambda_c$ in reciprocal space [15], the Chern number becomes a very useful tool [36]. The strategy is to cage the Weyl nodes inside a closed surface in reciprocal space, for example a sphere, $S^2$, of radius $k_c \sim 1/\lambda_c$, and then to calculate the flux of the Berry curvature, $\boldsymbol{\mathcal{F}}(\mathbf{k})$,

$$\mathcal{C}(\lambda) = \frac{1}{4\pi} \oint_{S^2} dS\, \hat{\mathbf{d}}(\mathbf{k}) \cdot (\boldsymbol{\nabla}_\theta \hat{\mathbf{d}}(\mathbf{k}) \times \boldsymbol{\nabla}_\phi \hat{\mathbf{d}}(\mathbf{k})). \tag{6}$$

The Chern number, $\mathcal{C}(\lambda)$, defined in Eq. (6) picks up a topological phase transition from $\mathcal{C}(\lambda) = +1$, for weak warping, $\lambda < \lambda_c$, to $\mathcal{C}(\lambda) = -2$, for strong warping, $\lambda > \lambda_c$, as shown in Fig. 2.

Although the momentum-to-real-space mapping in Ref. [15] is universal, it becomes clearer in the chiral limit, $d_z = 0$, when $\sigma_z \mathcal{H}_0 \sigma_z = -\mathcal{H}_0$ and $\mathcal{H}_0$ is off-diagonal [37]. By writing $d_\pm(\mathbf{k}) = |\mathbf{d}(\mathbf{k})| e^{\pm i\phi_\mathbf{k}}$, the original eigenstates (4) simplify to

$$|u_\mathbf{k}^\pm\rangle = \frac{1}{\sqrt{2}} \begin{bmatrix} e^{\mp i\phi_\mathbf{k}} \\ 1 \end{bmatrix}, \tag{7}$$

with $\phi_\mathbf{k} = \arg(\mathbf{d}(\mathbf{k})) \equiv \arctan(d_y(\mathbf{k})/d_x(\mathbf{k}))$. The $\mathbf{k}-$space vortex in (7) is such that for any closed adiabatic path encircling the Weyl nodes, the winding of the Berry phase is [15]

$$-i \oint d\phi_\mathbf{k} \langle u_\mathbf{k} | \nabla_{\phi_\mathbf{k}} | u_\mathbf{k} \rangle = \ell\pi. \tag{8}$$

Following Ref. [38], we now construct a wave packet with the aid of an envelope, $a(\mathbf{k})$, of width set by the radius $k_c$ of the

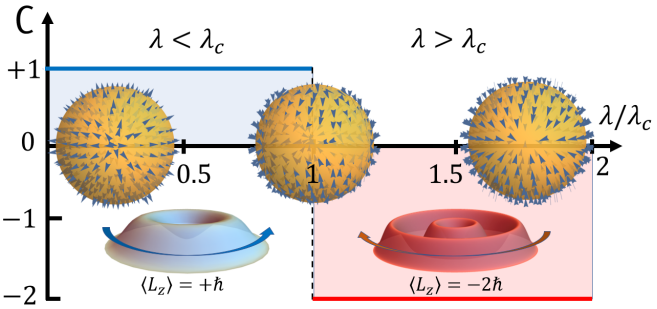


FIG. 2. Chern number, $\mathcal{C}(\lambda)$, versus warping, $\lambda/\lambda_c$, from Eq. (6). The yellow spheres represent the cage, $S^2$, in reciprocal space with radius set by the inverse Compton wavelength, $k_c \sim 1/\lambda_c$. The arrows piercing the cage outwards or inwards represent the Berry curvature, $\boldsymbol{\mathcal{F}}(\mathbf{k})$, that is integrated out in Eq. (6). For $\lambda/\lambda_c < 1$, a single Weyl node $Q = +1$ is inside the cage and $\mathcal{C} = +1$. The (blue) Bessel wave packet rotates counterclockwise, with $\langle L_z\rangle = +\hbar$. For $\lambda/\lambda_c > 1$, all four nodes $Q = +1, -1, -1, -1$ are inside the cage and $\mathcal{C} = -2$. The (red) Bessel wave packet rotates clockwise, with $\langle L_z\rangle = -2\hbar$.

cage

$$|W\rangle = \int \frac{d^d\mathbf{k}}{(2\pi)^d}\, a(\mathbf{k})\, e^{i\mathbf{k}\cdot(\mathbf{r}-\mathbf{r}_c)}|u_\mathbf{k}\rangle, \tag{9}$$

where $\mathbf{r}_c$ is the wave packet center of mass. For a paraxial wave packet, the scalar wave function acquires the Bessel form [38], $\psi_\ell \sim e^{i\ell\phi}J_\ell(k_\perp\rho)$, with $k_\perp = \sqrt{k_x^2 + k_y^2}$ and $\rho = \sqrt{x^2+y^2}$, and a Hilbert factor, $e^{i\ell\phi}$, such that $\langle L_z\rangle = \ell\hbar$, shown as insets in Fig. 2. For $\lambda < \lambda_c$, a single Weyl node $Q = +1$ is adiabatically encircled in Eq. (8), the Chern number, $\mathcal{C} = +1$, generates $\ell = +1$ and the (blue) Bessel wave packet rotates counterclockwise with $\langle L_z\rangle = +\hbar$, see Fig. 2 (inset: bottom left). For $\lambda > \lambda_c$, however, all four Weyl nodes $Q = +1, -1, -1, -1$ are adiabatically encircled in Eq. (8), the Chern number, $\mathcal{C} = -2$, generates $\ell = -2$ and the (red) Bessel wave packet rotates clockwise with $\langle L_z\rangle = -2\hbar$, see Fig. 2 (inset: bottom right).

## III. MANIPULATION AND QUENCHING

The semiclassical dynamics describing the motion of a rotating wave packet in the presence of electromagnetic fields was developed in Refs. [39–41]. Uniform electric, $\mathbf{E}$, and magnetic, $\mathbf{B}$, fields can be added to the Hamiltonian (1) as usual through both a scalar, $\phi(\mathbf{r})$ and a vector, $\mathbf{A}(\mathbf{r})$, potentials

$$\begin{aligned}\mathbf{E} &= -\nabla\phi(\mathbf{r}) - \frac{\partial\mathbf{A}(\mathbf{r})}{\partial t},\\ \mathbf{B} &= \nabla\times\mathbf{A}(\mathbf{r}).\end{aligned} \tag{10}$$

For nonzero Berry connection, $\boldsymbol{\mathcal{R}}$, and Berry curvature, $\boldsymbol{\mathcal{F}}$, the dynamics of the center of mass is described by

$$\begin{aligned}\hbar\dot{\mathbf{k}}_c &= -e\mathbf{E} - e\dot{\mathbf{r}}_c\times\mathbf{B},\\ \hbar\dot{\mathbf{r}}_c &= -i\boldsymbol{\eta}^\dagger[i\nabla_{\mathbf{k}_c} + \boldsymbol{\mathcal{R}}, \mathcal{H}_0]\boldsymbol{\eta} - \hbar\dot{\mathbf{k}}_c\times\boldsymbol{\eta}^\dagger\boldsymbol{\mathcal{F}}\boldsymbol{\eta},\end{aligned} \tag{11}$$

where $\dot{\mathbf{k}}_c$ and $\dot{\mathbf{r}}_c$ are the acceleration and velocity of the center of mass and $\boldsymbol{\eta}$ is the spinor component. The magnetization dynamics relative to the center of mass is described by [41]

$$i\hbar\dot{\boldsymbol{\eta}} = \Big(\frac{e}{2m}\boldsymbol{\mathcal{L}}\cdot\mathbf{B} - \hbar\dot{\mathbf{k}}_c\cdot\boldsymbol{\mathcal{R}}\Big)\boldsymbol{\eta}, \tag{12}$$

where for a relativistic particle of charge $e$ and mass $m$, the size of the Compton wavelength, $\lambda_c$, and with dilation factor $\gamma$ [39,40]

$$\boldsymbol{\mathcal{L}}(\mathbf{k}) = \frac{\hbar}{\gamma^2}\left(\sigma + \lambda_c^2\frac{\mathbf{k}\cdot\sigma}{\gamma+1}\mathbf{k}\right), \tag{13}$$

is the angular momentum operator including the helicity. The full Hamiltonian describing the motion of a rotating, relativistic wave packet is, therefore, the sum of a Bloch energy, an electrostatic energy, and a Zeeman energy [41]

$$\mathcal{H}(\mathbf{r}_c,\mathbf{k}_c) = \mathcal{H}_0(\mathbf{k}_c + e\mathbf{A}(\mathbf{r}_c)) - e\phi(\mathbf{r}_c) + \frac{e}{2m}\boldsymbol{\mathcal{L}}(\mathbf{k}_c)\cdot\mathbf{B}. \tag{14}$$

In this expression, $\mathcal{H}_0(\mathbf{k}_c + e\mathbf{A}(\mathbf{r}_c))$ includes all magnetic phenomena associated to the center of mass of the wave packet, $\mathbf{r}_c(B)$ and $\mathbf{k}_c(B)$, generated by Peierls substitution, $\mathbf{k}_c \to \mathbf{k}_c + e\mathbf{A}(\mathbf{r}_c)$. The presence of a nonzero vector potential, $\mathbf{A}(\mathbf{r}_c) \neq 0$, produces very interesting and well studied physical phenomena, such as Lorentz forces, cyclotron orbits, and Landau levels, which have already been thoroughly studied and whose theory for the magnetic susceptibility due to $\mathcal{H}_0(\mathbf{k}_c + e\mathbf{A}(\mathbf{r}_c))$ is reviewed in Ref. [42]. In what follows, however, we shall, instead, discuss the contribution from the rotation of the wave packet, namely, phenomena *relative to the center of mass*, which corresponds precisely to the Zeeman Hamiltonian, $\mathcal{H}_Z = (e/2m)\boldsymbol{\mathcal{L}}(\mathbf{k}_c)\cdot\mathbf{B}$, in Eq. (14).

Let us now consider the case of a nonzero, transverse magnetic field, $\mathbf{B}\perp\hat{z}$, and zero electric field, $\phi(\mathbf{r}_c) = constant$, in the Coulomb gauge, $\nabla\cdot\mathbf{A}(\mathbf{r}_c) = 0$ and $\partial\mathbf{A}(\mathbf{r}_c)/\partial t = 0$. For Bloch electrons at long wavelengths we have $\gamma \approx 1$ and therefore $\boldsymbol{\mathcal{L}} = -\hbar\sigma$ [39]. Recalling the definition $\mu_B = e\hbar/2m$, we conclude that

$$\mathcal{H}_Z = -\mu_B\sigma\cdot\mathbf{B}, \tag{15}$$

modifies the positions of all Weyl nodes [43], so that the magnetic texture, $\mathbf{m}_\pm(\mathbf{k}) = \langle u_\mathbf{k}^\pm|\boldsymbol{\sigma}|u_\mathbf{k}^\pm\rangle$, becomes aligned with $\mathbf{B}$. Inserting $\mathbf{d}(\mathbf{k},\mathbf{B}) = \mathbf{d}(\mathbf{k}) - \mu_B\mathbf{B}$ into Eq. (2) we can use once again the Chern number, $\mathcal{C}(\lambda, B)$, to produce the $\lambda\times B$ topological phase diagram shown in Fig. 3, for a magnetic field at an angle $\theta = \pi/3$ with the $x$–axis. In what follows, we will measure $\mathbf{B}$ in units of $\mu_B$.

At $\mathbf{B} = 0$ and $\lambda > \lambda_c$, we have $\mathcal{C}(\lambda, 0) = -2$. All four nodes are inside the cage, see Fig. 3, and the rotating wave packet has angular momentum $\langle L_z\rangle = -2\hbar$. As the magnetic field increases, we observe, initially, the annihilation between the central node, $Q = +1$, and one of its satellites, $Q = -1$, without changing the Chern number. This occurs when the magnetic length, $l_B^{-1} = \sqrt{eB/\hbar}$, becomes comparable to the node separation [44] and the magnetic tunneling between nodes of opposite chirality is promoted [45]. Further increase in the magnetic field causes a partial quench, $\mathcal{C} = -2 \to -1$, when one of the satellite nodes with $Q = -1$ leaves the cage, see Fig. 3, and the angular momentum of the rotating wave packet becomes $\langle L_z\rangle = -\hbar$. Finally, at even higher fields the

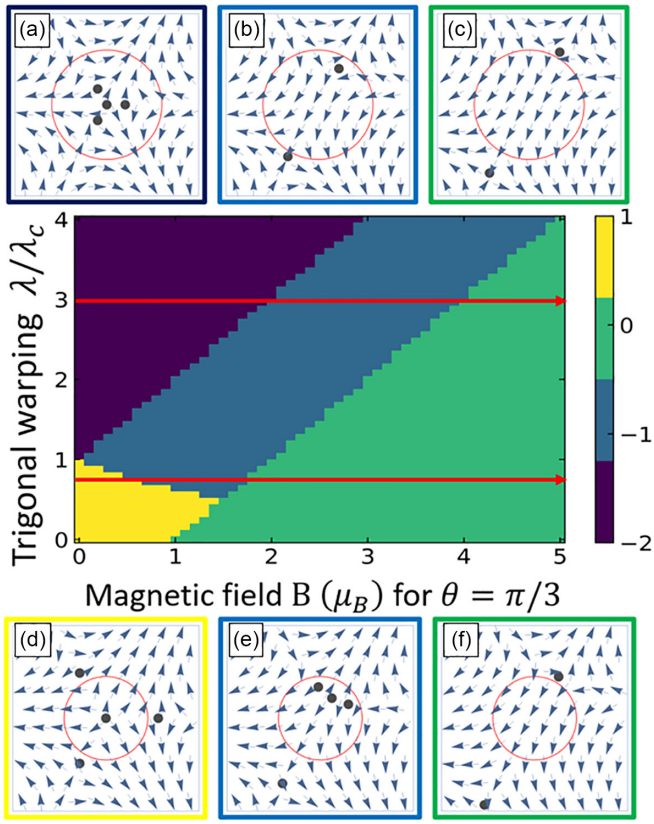


FIG. 3. Topological phase diagram for the Hamiltonian (1) in a transverse magnetic field, $\mathbf{B} \perp \hat{z}$. The six square panels depict the $x, y$ components of the orbital magnetic texture (5) for strong (top) and weak (bottom) warping, at $\theta = \pi/3$, which is a high-symmetry angle (halfway a $C_3$ operation). The black dots on all six satellite square panels represent the Weyl nodes with respect to the cage, represented by the thin red circle. Top: in the strong band warping case, $\lambda_W \equiv \lambda/\lambda_c = 3.0$ (top horizontal red arrow in the main panel), one observes a two-step topological transition depicted in (a) $\rightarrow$ (b) $\rightarrow$ (c). First there is a partial quenching of the wave-packet rotation, $\mathcal{C} = -2 \rightarrow -1$, and then its complete quenching, $\mathcal{C} = -1 \rightarrow 0$. Bottom: in the weak band warping case, $\lambda_W \equiv \lambda/\lambda_c = 0.8$ (bottom horizontal red arrow in the main panel), one observes also a two-step topological transition depicted in (d) $\rightarrow$ (e) $\rightarrow$ (f). First there is a reversal in the direction of rotation of the wave packet, $\mathcal{C} = +1 \rightarrow -1$, and then its complete quenching, $\mathcal{C} = -1 \rightarrow 0$. The frame color of each box follows the color assigned to each topological sector in the color bar of the phase diagram.

wave packet rotation is completely quenched, $\mathcal{C} = -1 \rightarrow 0$, after all satellite nodes have left the cage and $\langle L_z \rangle = 0$, see Fig. 3. Variations of the angle $0 \leqslant \theta_{xy} \leqslant 2\pi$ produce the polar phase diagrams shown in Fig. 4, which exhibits the $C_3$ symmetry of the Hamiltonian (1). Notice that for $\lambda < \lambda_c$ there exists a transition $\mathcal{C} = +1 \rightarrow -1 \rightarrow 0$, which corresponds to a single node with $Q = +1$ initially inside the cage at zero field which is joined by two of its satellites with $Q = -1$ each, see Fig. 3. One of the satellites annihilates with the central one, while the other is expelled from the cage at high fields. The angular momentum $\langle L_z \rangle = +\hbar$ is first reversed to $\langle L_z \rangle = -\hbar$ before it is completely quenched, $\langle L_z \rangle = 0$.

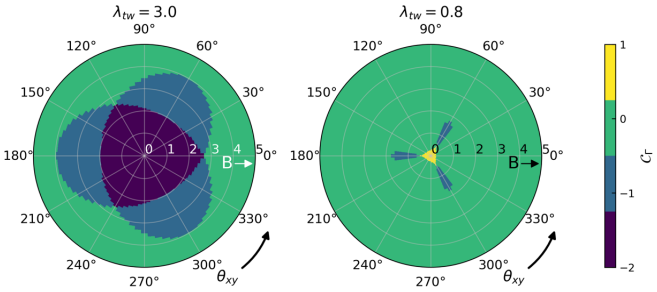


FIG. 4. Polar plots of the topological phase diagram in Fig. 3. (Left): for strong band warping, $\lambda_W \equiv \lambda/\lambda_c = 3.0$, corresponding to the top horizontal red arrow in Fig. 3 and (a) $\rightarrow$ (b) $\rightarrow$ (c). (Right): weak band warping, $\lambda_W = 0.8$, corresponding to the bottom horizontal red arrow in Fig. 3 and (d) $\rightarrow$ (e) $\rightarrow$ (f). The applied magnetic field varies between $B = 0 \rightarrow 5(\mu_B)$, and for $0 \leqslant \theta_{xy} \leqslant 2\pi$.

## IV. STEPS AND PLATEAUS IN THE 3D QAHE

Hamiltonian (1) has recently been successfully used to describe several magnetotransport and Hall responses in trigonally warped tellurium [46]. The topological transitions discussed above are bound to leave unique fingerprints in any wave-packet-related properties, such as the intrinsic [47] or the nonlinear [48] anomalous Hall conductivities, $\sigma_{xy}(\varepsilon)$, or the $z$ magnetization

$$\mathcal{M}_z = \int \frac{d^3\mathbf{k}}{(2\pi)^3} f(\mathbf{k}) m_z(\mathbf{k}) + \frac{1}{e} \int d\varepsilon f(\varepsilon)\, \sigma_{xy}(\varepsilon), \qquad (16)$$

where $f(\varepsilon)$ is the particle distribution function and $\varepsilon$ is the energy. The first term in Eq. (16) is a smooth bulk contribution from $\mathbf{m}(\mathbf{k})$ while the second term is a quantized, surface contribution from the anomalous Hall effect [41]. In equilibrium both contributions to Eq. (16) are identically zero by symmetry, but an electric field, $\mathbf{E}$, can induce a net smooth contribution to $\mathcal{M}_z$ [49–51], see Fig. 5(a). The center of mass distribution is governed by

$$\frac{\partial f}{\partial t} + \dot{\mathbf{r}}_c \cdot \nabla_{\mathbf{r}_c} f + \dot{\mathbf{k}}_c \cdot \nabla_{\mathbf{k}_c} f = -\frac{f - f^{(0)}}{\tau} \equiv -\frac{\delta f}{\tau}, \qquad (17)$$

with $\dot{\mathbf{r}}_c$ and $\dot{\mathbf{k}}_c$ defined in Eq. (11), $\tau$ is a relaxation time, and $f(\mathbf{r}_c, \mathbf{k}_c, t)$ ($f^{(0)}(\mathbf{r}_c, \mathbf{k}_c, t)$) is the nonequilibrium

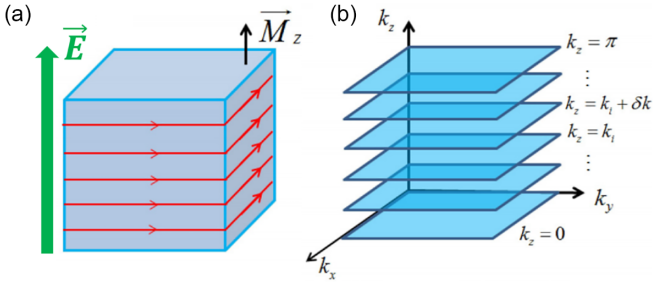


FIG. 5. (a) the electric-field induced magnetization, $M_z(\mathbf{E})$, via Edelstein effect [52] and chiral surface sheet states; (b) adiabatically connected slices, $k_i$, perpendicular to $k_z$ [53], all with the same Chern number [36].

(equilibrium) distribution, such that

$$\delta f(\mathbf{k}, \mathbf{E}) = -(\dot{\mathbf{r}}_c(\mathbf{k})\tau) \cdot (e\mathbf{E})(\partial_\varepsilon f^{(0)}(\mathbf{k})), \tag{18}$$

and $f^{(0)}(\mathbf{k}) = 1/(e^{\beta(\varepsilon(\mathbf{k})-\mu)} + 1)$ is Fermi-Dirac's distribution function for energy dispersion, $\varepsilon(\mathbf{k})$, at the chemical potential, $\mu$, and inverse temperature, $\beta = 1/k_B T$.

Because of the texture-momentum locking in Eq. (5), $\mathbf{m}(\mathbf{k})$, the applied field, $\mathbf{E} \parallel \hat{z}$, generates an imbalance between positive and negative $k_z$ components of $\mathbf{m}(\mathbf{k})$, producing a field-induced magnetization. This phenomenon is known as the Edelstein effect [52] and has been observed in several materials and model systems [49–51], in which a net magnetization, $M_z(\mathbf{E})$, is generated by an applied electric field, $\mathbf{E} \parallel \hat{z}$, according to

$$M_z(\mathbf{E}) \equiv \int d\mathbf{k}\, m_z(\mathbf{k})\, \delta f(\mathbf{k}, \mathbf{E}) \neq 0. \tag{19}$$

The induced magnetization, $M_z(\mathbf{E})$, in turn, breaks time-reversal symmetry, gaps the spectrum, and transforms the semimetal into a Chern (quantum anomalous Hall) insulator, with chiral surface sheet states, see Fig. 5(a). The Chern numbers $C_1, \ldots, C_N$, associated with the slices orthogonal to the $k_z$ direction from $k_z = 0$ to $k_z = \pi$, shown in Fig. 5(b), are all equal [36]. This is because planes at momenta $k_z$ and $k_z + \delta k$ can be adiabatically connected without closing the gap [53]. Hence, if any 2D cut with a given Chern number, $\mathcal{C}$, is identified, this material must be a 3D quantum anamolus Hall effect (QAHE) insulator [53]. For that reason we calculate the 2D Hall conductance at $k_z = 0$ for the wave packet (9) following the procedure described in [47]:

$$\sigma_{xy}^{2D}(\varepsilon, \mathbf{B}) = \frac{e^2}{2\pi\hbar} \int_{|\mathbf{k}|<\Lambda} d^2\mathbf{k}\, \mathcal{F}_{xy}(\mathbf{k}, \mathbf{B})\, g(\mathbf{k}, \varepsilon, \mathbf{B}), \tag{20}$$

where

$$\mathcal{F}_{xy}(\mathbf{k}, \mathbf{B}) = \hat{\mathbf{d}}(\mathbf{k}, \mathbf{B}) \cdot (\nabla_{k_x} \hat{\mathbf{d}}(\mathbf{k}, \mathbf{B}) \times \nabla_{k_y} \hat{\mathbf{d}}(\mathbf{k}, \mathbf{B}))$$

and

$$g(\mathbf{k}, \varepsilon, \mathbf{B}) = \int d\mathbf{k}' f(\varepsilon - |\mathbf{d}(\mathbf{k}', \mathbf{B})|)\, |a(\mathbf{k} - \mathbf{k}')|^4, \tag{21}$$

which has a compact support acting as a cage for the Berry curvature, $\mathcal{F}_{xy}(\mathbf{k}, \mathbf{B})$, and whose shape and position in $\mathbf{k}$ space are determined by the magnetic field, $\mathbf{B}$, and energy, $\varepsilon$. The ultraviolet (UV) cutoff, $\Lambda$, in Eq. (20) is a material specific property that sets the scale for $\mathbf{k}$ above which the long-wavelength, infrared (IR) description (1) of the (now) $2 \times 2$ chiral Dirac Fermions breaks down. For $|\mathbf{k}| > \Lambda$, the dispersion relation bends towards the boundaries of the Brillouin zone, becoming less dispersive thus producing electronic states with a rather large effective mass at very short wavelengths, also known as *spectator Fermions* [54,55].

In Fig. 6(a) we show $\sigma_{xy}^{2D}(\varepsilon, \mathbf{B} = 0)$ for $\lambda < \lambda_c$ (blue), where $\mathcal{C} = +1$, and $\lambda > \lambda_c$ (red), where $\mathcal{C} = -2$. The conductivity is nearly half-quantized, $\sigma_{xy}^{2D}(0, 0) \approx \mathcal{C}e^2/2\hbar$, and the width of the plateaus is determined by $M_z$. For an initial $\lambda \gg \lambda_c$ and $\mathbf{B} \perp \hat{z}$, the wave packet becomes quenched and the plateau of the anomalous Hall conductivity, $\sigma_{xy}^{2D}(0, \mathbf{B})$, crosses over markedly between $-2e^2/2\hbar \to -1e^2/2\hbar \to 0$, see Fig. 6(b). The stepwise quenching of the wave-packet

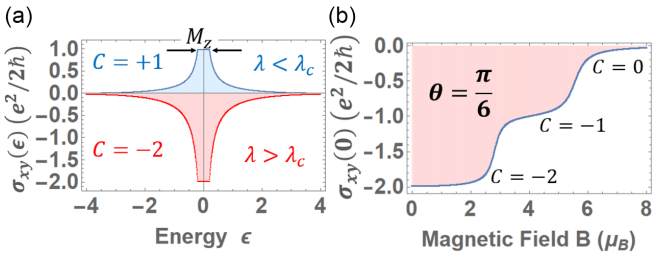


FIG. 6. (a) zero field, 2D Hall conductivity, $\sigma_{xy}^{2D}(\varepsilon)$, for $\lambda < \lambda_c$ (blue), where $\mathcal{C} = +1$ and the wave packet rotates clockwise with orbital angular momentum $\langle L_z \rangle = +\hbar$, and $\lambda > \lambda_c$ (red), where $\mathcal{C} = -2$ and the wave packet rotates clockwise with orbital angular momentum $\langle L_z \rangle = -2\hbar$; (b) 2D Hall plateaus, $\sigma_{xy}^{2D}(0, \mathbf{B})$, as a function of the applied magnetic field (example for $\theta = \pi/6$) showing a step-wise structure reflecting the the two-step magnetic quenching of the wave packet orbital angular momentum, for $\lambda > \lambda_c$.

rotation is depicted in Fig. 7. The absence of sharp discontinuities results from the nonsingular character of the Berry curvature, $\mathcal{F}_{xy}(\mathbf{k}, \mathbf{B})$, when $M_z \neq 0$, and from the uncertainty, $\Delta\mathbf{k}$, brought in by the finite spread of the envelope $a(\mathbf{k})$. The transitions occur when the cages fail to enclose regions of nonzero Berry curvature, for $|\mathbf{k}| < \Lambda$. In Fig. 8, we plot the Berry curvature, $\mathcal{F}_{xy}(\mathbf{k}, \mathbf{B})$, the cage, $g(\mathbf{k}, \varepsilon, \mathbf{B})$, and the UV cutoff, $\Lambda$, used in the calculation of $\sigma_{xy}^{2D}$, for different values of $\lambda$ and $\mathbf{B}$. The angular momentum lost by the IR Fermions is, however, transferred to the UV *spectator Fermions*, so that the total topological charge inside the entire Brillouin zone is preserved, $\Delta\mathcal{C}_{IR} + \Delta\mathcal{C}_{UV} = 0$, as expected.

In order to test our predictions some estimates need to be provided. Hamiltonian (1) can either occur on its own, as a main contribution [28], or, as often, it occurs as a correction to some underlying, high-symmetry band dispersion, $(\hbar^2/2m_\perp^*)\mathbf{k}_\perp^2 + (\hbar^2/2m_\parallel^*)\mathbf{k}_\parallel^2$ [32]. According to Eq. (19), an electric field, $E_z \sim 10^4 V/m$, applied to $10^{16} - 10^{18}\text{cm}^{-3}$ free carriers, generates a net magnetization between $M_z \sim 10 - 1000$ Gauss, for $\tau \sim 10^{-12} s$ and an effective mass $m_{\perp,\parallel}^* \sim 0.1 - 0.4\, m_e$ [50,51]. For systems with trigonal warping, the satellite nodes typically occur at arround $k_{tw} \sim 10^6\text{cm}^{-1}$ from a high symmetry axis [28,30]. Recalling that for topological insulators and semiconductors, $E_g \sim 0.1 - 0.5$ eV, the typical Compton wavelength of a semirelativistic wave packet is of the order of $\lambda_c \sim 10 - 50$ Å [56], we conclude that for a field induced, time-reversal breaking topological gap of $\Delta \sim 1 - 3$ meV and at $T \sim 10$ K, the intensity of the transverse

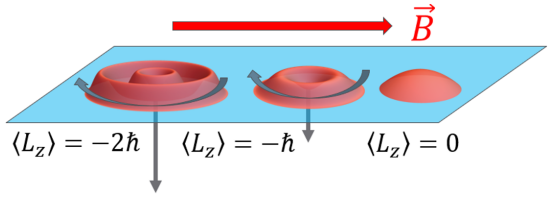


FIG. 7. Step-wise quenching of the orbital rotation of the wave packet for $\lambda > \lambda_c$ and an applied, transverse magnetic field. The rotation, initially with orbital angular momentum $\langle L_z \rangle = -2\hbar$ is first partially quenched to an orbital angular momentum $\langle L_z \rangle = -\hbar$, and then completely quenched to an orbital angular momentum $\langle L_z \rangle = 0$.

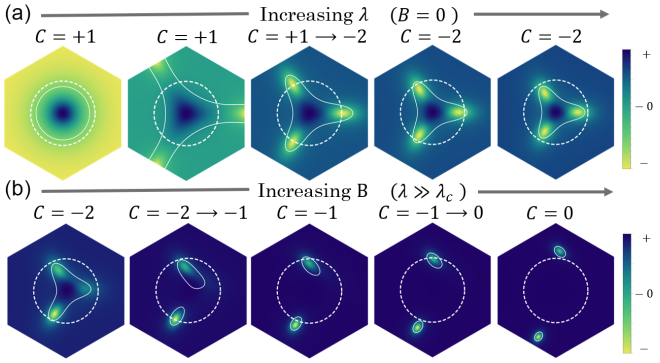


FIG. 8. Density plot of the Berry curvature, $\mathcal{F}_{xy}(\mathbf{k}, \mathbf{B})$, $\mathbf{k}-$space cages, $g(\mathbf{k}, \varepsilon, \mathbf{B})$ (solid white lines) with $\varepsilon > |M_z|$, and ultraviolet cutoff $|\mathbf{k}| < \Lambda$ (dashed white lines), inside the surroundings of a high symmetry point in the Brillouin zone. Top row: $\mathbf{B} = 0$ and increasing $\lambda$, showing $\mathcal{C} = +1 \to -2$; Bottom row: fixed $\lambda \gg \lambda_c$ and increasing $\mathbf{B}$, showing $\mathcal{C} = -2 \to -1 \to 0$, for $\theta = \pi/6$.

magnetic field necessary to induce such topological transitions is of the order $B = 1 - 5$ T, is well within the accessible range of typical laboratory equipments.

## V. CONCLUSIONS

This work constitutes a fundamental building block to the emergent field of Weyl magnetronics: the control of charge through the magnetic manipulation of Weyl nodes and wave packets, in order to fine-tune the 3D quantum anomalous Hall effect. We also predict the existence of discretized anomalous Hall plateaus due to the wave packet rotation, even in the absence of Landau levels. Candidate Weyl magnetronic materials include monolayer and twisted bilayer graphene [28,29], monolayer $MoS_2$ [31], and $Bi_2Te_3$ [34]. In particular, the possibility of manipulation of Weyl nodes in elemental tellurium via strain (Weyl straintronics), numerically reported in Ref. [57], encourages the pursuit for the Weyl magnetronics in that very system, which might reveal the quantization of the intrinsic [47] and nonlinear [48] anomalous Hall effects, or any other observables sensitive to the Weyl node position or the structure of van Hove singularities in the electronic structure [58].

## ACKNOWLEDGMENTS

The authors acknowledge support from CNPq - INCT (National Institute of Science and Technology on Materials Informatics), Grant No. 371610/2023-0, and from FAPESP (Fundação de Amparo à Pesquisa do Estado de São Paulo), Grant No. 2023/06522-0.

[1] H. Kragh, Wave packet, in *Compendium of Quantum Physics*, edited by D. Greenberger, K. Hentschel, and F. Weinert (Springer, Berlin, 2009), pp. 828–830.
[2] E. Schrödinger, Der stetige Übergang von der Mikro- zur Makromechanik, Naturwissenschaften **14**, 664 (1926).
[3] L. de Broglie, XXXV. A tentative theory of light quanta, London, Edinburgh Dublin Philos. Mag. J. Sci. **47**, 446 (1924).
[4] L. Hall and A. Abouraddy, Observation of optical de Broglie-Mackinnon wave packets, Nat. Phys. **19**, 435 (2023).
[5] M. Yessenov, J. Free, Z. Chen, E. G. Johnson, M. P. J. Lavery, M. A. Alonso, and A. F. Abouraddy, Space-time wave packets localized in all dimensions, Nat. Commun. **13**, 4573 (2022).
[6] S. Sheng, A.-C. Oeter, M. Abdo, K. Lichtenberg, M. Hentschel, and S. Loth, Launching coherent acoustic phonon wave packets with local femtosecond Coulomb forces, Phys. Rev. Lett. **129**, 043001 (2022).
[7] Y.-X. Shen, R. Lirette, and L. Zhang, Ultrasonic super-oscillation wavepackets with an acoustic meta-lens, Nat. Commun. **10**, 3411 (2019).
[8] K. Akbari, V. D. Giulio, and F. J. G. de Abajo, Optical manipulation of matter waves, Sci. Adv. **8**, eabq2659 (2022).
[9] Y. Shen, X. Wang, Z. Xie, C. Min, X. Fu, Q. Liu, M. Gong, and X. Yuan, Optical vortices 30 years on: Oam Manipulation from topological charge to multiple singularities, Light: Sci. Appl. **8**, 90 (2019).
[10] M. Brambilla, F. Battipede, L. A. Lugiato, V. Penna, F. Prati, C. Tamm, and C. O. Weiss, Transverse laser patterns. I. Phase singularity crystals, Phys. Rev. A **43**, 5090 (1991).
[11] S. Coh, Classification of materials with phonon angular momentum and microscopic origin of angular momentum, Phys. Rev. B **108**, 134307 (2023).
[12] Z. Zou, R. Lirette, and L. Zhang, Orbital angular momentum reversal and asymmetry in acoustic vortex beam reflection, Phys. Rev. Lett. **125**, 074301 (2020).
[13] S. M. Lloyd, M. Babiker, G. Thirunavukkarasu, and J. Yuan, Electron vortices: Beams with orbital angular momentum, Rev. Mod. Phys. **89**, 035004 (2017).
[14] K. Y. Bliokh, P. Schattschneider, J. Verbeeck, and F. Nori, Electron vortex beams in a magnetic field: A new twist on Landau levels and Aharonov-Bohm states, Phys. Rev. X **2**, 041011 (2012).
[15] X. Liu, S. Xia, D. Song, D. Li, L. Tang, D. Leykam, J. Xu, H. Buljan, and Z. Chen, Universal momentum-to-real-space mapping of topological singularities, Nat. Commun. **11**, 1586 (2020).
[16] K. Y. Bliokh, M. A. Alonso, E. A. Ostrovskaya, and A. Aiello, Angular momenta and spin-orbit interaction of non-paraxial light in free space, Phys. Rev. A **82**, 063825 (2010).
[17] H. Nielsen and M. Ninomiya, Absence of neutrinos on a lattice: (II). Intuitive topological proof, Nucl. Phys. B **193**, 173 (1981).
[18] M. M. Piva, J. C. Souza, V. Brousseau-Couture, S. Sorn, K. R. Pakuszewski, J. K. John, C. Adriano, M. Côté, P. G. Pagliuso, A. Paramekanti, and M. Nicklas, Topological features in the ferromagnetic Weyl semimetal CeAlSi: Role of domain walls, Phys. Rev. Res. **5**, 013068 (2023).
[19] D. Destraz, L. Das, S. S. Tsirkin, Y. Xu, T. Neupert, J. Chang, A. Schilling, A. G. Grushin, J. Kohlbrecher, L. Keller, P. Puphal, E. Pomjakushina, and J. S. White, Magnetism and anomalous transport in the Weyl semimetal PrAlGe: possible route to axial gauge fields, npj Quantum Mater. **5**, 5 (2020).

[20] F. Abdulla, A. Das, S. Rao, and G. Murthy, Time-reversal-broken Weyl semimetal in the Hofstadter regime, SciPost Phys. Core **5**, 014 (2022).

[21] J. Shen, J. Gao, C. Yi, M. Li, S. Zhang, J. Yang, B. Wang, M. Zhou, R. Huang, H. Wei, H. Yang, Y. Shi, X. Xu, H.-J. Gao, B. Shen, G. Li, Z. Wang, and E. Liu, Magnetic-field modulation of topological electronic state and emergent magneto-transport in a magnetic Weyl semimetal, The Innovation **4**, 100399 (2023).

[22] E. Cheng, L. Yan, X. Shi, R. Lou, A. Fedorov, M. Behnami, J. Yuan, P. Yang, B. Wang, J.-G. Cheng, Y. Xu, Y. Xu, W. Xia, N. Pavlovskii, D. C. Peets, W. Zhao, Y. Wan, U. Burkhardt, Y. Guo, S. Li, C. Felser, W. Yang, and B. Büchner, Tunable positions of Weyl nodes via magnetism and pressure in the ferromagnetic Weyl semimetal CeAlSi, Nat. Commun. **15**, 1467 (2024).

[23] B. Sadhukhan and T. Nag, Effect of chirality imbalance on Hall transport of $PrRhC_2$, Phys. Rev. B **107**, L081110 (2023).

[24] B. Q. Lv, H. M. Weng, B. B. Fu, X. P. Wang, H. Miao, J. Ma, P. Richard, X. C. Huang, L. X. Zhao, G. F. Chen, Z. Fang, X. Dai, T. Qian, and H. Ding, Experimental discovery of Weyl semimetal TaAs, Phys. Rev. X **5**, 031013 (2015).

[25] C. Fang, M. J. Gilbert, X. Dai, and B. A. Bernevig, Multi-Weyl topological semimetals stabilized by point group symmetry, Phys. Rev. Lett. **108**, 266802 (2012).

[26] W.-J. Chen, M. Xiao, and C. Chan, Photonic crystals possessing multiple Weyl points and the experimental observation of robust surface states, Nat. Commun. **7**, 13038 (2016).

[27] T. Nag, A. Menon, and B. Basu, Thermoelectric transport properties of Floquet multi-Weyl semimetals, Phys. Rev. B **102**, 014307 (2020).

[28] P. Rakyta, A. Kormányos, and J. Cserti, Trigonal warping and anisotropic band splitting in monolayer graphene due to Rashba spin-orbit coupling, Phys. Rev. B **82**, 113405 (2010).

[29] P. Mohan, U. Ghorai, and R. Sensarma, Trigonal warping, satellite Dirac points, and multiple field tuned topological transitions in twisted double bilayer graphene, Phys. Rev. B **103**, 155149 (2021).

[30] J. M. Adhidewata, R. W. M. Komalig, M. S. Ukhtary, A. R. T. Nugraha, B. E. Gunara, and E. H. Hasdeo, Trigonal warping effects on optical properties of anomalous Hall materials, Phys. Rev. B **107**, 155415 (2023).

[31] A. Kormányos, V. Zólyomi, N. D. Drummond, P. Rakyta, G. Burkard, and V. I. Fal'ko, Monolayer $MoS_2$: Trigonal warping, the Γ′ valley, and spin-orbit coupling effects, Phys. Rev. B **88**, 045416 (2013).

[32] T. Doi, K. Nakao, and H. Kamimura, The valence band structure of tellurium. I. The $k{\cdot}p$ perturbation method, J. Phys. Soc. Jpn. **28**, 36 (1970).

[33] G. P. Maruggi, J. Ferreira, E. Baggio-Saitovitch, C. Enderlein, and M. B. Silva Neto, Hedgehog orbital texture in *p*-type tellurium and the antisymmetric nonreciprocal Hall response, Phys. Rev. Mater. **7**, 014204 (2023).

[34] I. Mohelský, A. Dubroka, J. Wyzula, A. Slobodeniuk, G. Martinez, Y. Krupko, B. A. Piot, O. Caha, J. Humlíček, G. Bauer, G. Springholz, and M. Orlita, Landau level spectroscopy of $Bi_2Te_3$, Phys. Rev. B **102**, 085201 (2020).

[35] D. Culcer, Y. Yao, and Q. Niu, Coherent wave-packet evolution in coupled bands, Phys. Rev. B **72**, 085110 (2005).

[36] D. Gresch, G. Autès, O. V. Yazyev, M. Troyer, D. Vanderbilt, B. A. Bernevig, and A. A. Soluyanov, Z2Pack: Numerical implementation of hybrid Wannier centers for identifying topological materials, Phys. Rev. B **95**, 075146 (2017).

[37] A. P. Schnyder, S. Ryu, A. Furusaki, and A. W. W. Ludwig, Classification of topological insulators and superconductors in three spatial dimensions, Phys. Rev. B **78**, 195125 (2008).

[38] K. Y. Bliokh, M. R. Dennis, and F. Nori, Relativistic electron vortex beams: Angular momentum and spin-orbit interaction, Phys. Rev. Lett. **107**, 174802 (2011).

[39] M.-C. Chang and Q. Niu, Berry curvature, orbital moment, and effective quantum theory of electrons in electromagnetic fields, J. Phys.: Condens. Matter **20**, 193202 (2008).

[40] C.-P. Chuu, M.-C. Chang, and Q. Niu, Semiclassical dynamics and transport of the Dirac spin, Solid State Commun. **150**, 533 (2010).

[41] D. Xiao, M.-C. Chang, and Q. Niu, Berry phase effects on electronic properties, Rev. Mod. Phys. **82**, 1959 (2010).

[42] G. P. Mikitik and Y. V. Sharlai, Magnetic susceptibility of topological nodal semimetals, Phys. Rev. B **94**, 195123 (2016).

[43] F. Dominguez, B. Scharf, and E. M. Hankiewicz, Crystalline Weyl semimetal phase in quantum spin Hall systems under magnetic fields, SciPost Phys. Core **5**, 024 (2022).

[44] F. Abdulla, Pairwise annihilation of Weyl nodes induced by magnetic fields in the Hofstadter regime, Phys. Rev. B **109**, 155142 (2024).

[45] C.-L. Zhang, S.-Y. Xu, C. M. Wang, Z. Lin, Z. Z. Du, C. Guo, C.-C. Lee, H. Lu, Y. Feng, S.-M. Huang, G. Chang, C.-H. Hsu, H. Liu, H. Lin, L. Li, C. Zhang, J. Zhang, X.-C. Xie, T. Neupert, M. Z. Hasan *et al.*, Magnetic-tunnelling-induced Weyl node annihilation in tap, Nat. Phys. **13**, 979 (2017).

[46] C.-H. Yin, H.-W. Fang, H.-T. Jiang, L. Cao, S. Han, Y.-Y. Lv, J. Zhou, S.-H. Yao, Z. K. Liu, Y. B. Chen, and Y.-F. Chen, Evolution of magnetotransport properties of Weyl semiconductor Te crystals with different Fermi energy, Phys. Rev. B **108**, 195121 (2023).

[47] V. Kozii, A. Avdoshkin, S. Zhong, and J. E. Moore, Intrinsic anomalous Hall conductivity in a nonuniform electric field, Phys. Rev. Lett. **126**, 156602 (2021).

[48] X. Liu, S. S. Tsirkin, and I. Souza, Covariant derivatives of Berry-type quantities: Application to nonlinear transport, arXiv:2303.10129.

[49] T. Furukawa, Y. Watanabe, N. Ogasawara, K. Kobayashi, and T. Itou, Current-induced magnetization caused by crystal chirality in nonmagnetic elemental tellurium, Phys. Rev. Res. **3**, 023111 (2021).

[50] T. Yoda, T. Yokoyama, and S. Murakami, Current-induced orbital and spin magnetizations in crystals with helical structure, Sci. Rep. **5**, 12024 (2015).

[51] V. A. Shalygin, A. N. Sofronov, L. E. Vorob'ev, and I. I. Farbshtein, Current-induced spin polarization of holes in tellurium, Phys. Solid State **54**, 2362 (2012).

[52] V. Edelstein, Spin polarization of conduction electrons induced by electric current in two-dimensional asymmetric electron systems, Solid State Commun. **73**, 233 (1990).

[53] Y. J. Jin, R. Wang, B. W. Xia, B. B. Zheng, and H. Xu, Three-dimensional quantum anomalous Hall effect in ferromagnetic insulators, Phys. Rev. B **98**, 081101(R) (2018).

[54] B. A. Bernevig, *Topological Insulators and Topological Superconductors* (Princeton University Press, Princeton, NJ, 2013).

[55] F. D. M. Haldane, Model for a quantum Hall effect without Landau levels: Condensed-matter realization of the "parity anomaly", Phys. Rev. Lett. **61**, 2015 (1988).

[56] W. Zawadzki, Semirelativity in semiconductors: A review, J. Phys.: Condens. Matter **29**, 373004 (2017).

[57] L. A. Agapito, N. Kioussis, W. A. Goddard, and N. P. Ong, Novel family of chiral-based topological insulators: Elemental tellurium under strain, Phys. Rev. Lett. **110**, 176401 (2013).

[58] P. Fontana, M. Burrello, and A. Trombettoni, Topological van Hove singularities at phase transitions in Weyl metals, Phys. Rev. B **104**, 195127 (2021).